

Tunable valley band and exciton splitting by interlayer orbital hybridization

Xiaolong Zou (✉ xlzou@sz.tsinghua.edu.cn)

Tsinghua University <https://orcid.org/0000-0002-3987-6865>

Dan Wang

Tsinghua University

Article

Keywords:

Posted Date: July 5th, 2022

DOI: <https://doi.org/10.21203/rs.3.rs-1775142/v1>

License:   This work is licensed under a Creative Commons Attribution 4.0 International License. [Read Full License](#)

Abstract

Magnetic proximity effect has been demonstrated to be an effective routine to introduce valley splitting in two-dimensional van der Waals heterostructures. However, the control of its strength and the induced valley splitting remains challenging. In this work, taking heterobilayers combining monolayer MSe_2 ($M = Mo$ or W) with room-temperature ferromagnetic VSe_2 as examples, we demonstrate that the valley splitting for both band edges and excitons can be modulated by the tuning of the interlayer orbital hybridization, achieved by inclusion of different amounts of exact Hartree exchange potential via hybrid functionals. The calculations suggest that large valley band splitting about 30 meV and valley exciton splitting over 150 meV can be induced in monolayer MSe_2 . Besides, we show such tuning of orbital hybridization could be experimentally realized by external strain. Our work reveals a way to control proximity effects and provides some guidance for the design of spintronic and valleytronic devices.

Introduction

Monolayer group VIB transition metal dichalcogenides (TMDs) with broken inversion symmetry and strong spin-orbit coupling (SOC) show intriguing coupled spin and valley phenomena¹⁻³. To address spin or valley degree of freedom, TMDs are usually selectively excited by circularly polarized light, leading to carriers/excitons with specific valley pseudospin. However, it is challenging to integrate light into electronic nanodevices. Another way is directly applying an external magnetic field to split the degenerate band edges with different valley pseudospins. Yet, the magnetic-field-induced splitting is only at the order of ~ 0.2 meV/T^{4,5}, showing limited promise in real applications. An alternative and robust approach is to build TMDs/magnets heterostructures taking advantage of the magnetic proximity effect, where the magnetic orders of magnets can significantly affect the behaviors of non-magnetic TMDs⁶⁻¹². Applying this strategy, it has been confirmed in experiments that the valley splittings of WSe_2 and WS_2 on top of bulk EuS reach 16 meV/T¹³ and 2.5 meV/T¹⁴, respectively. When two-dimensional (2D) ferromagnetic semiconductor CrI_3 and $CrBr_3$ were adopted as substrates, splittings about 4 meV for WSe_2 ¹⁵ and 2.9 meV for $MoSe_2$ ¹⁶ have been realized.

Although several prototypical magnetic proximity systems have been studied, achieving a large valley splitting in 2D heterostructures is still in demand, which requires a general understanding on the strength and influencing factors of magnetic proximity effect, as well as its consequences on excitonic properties. To achieve this goal, model systems with commensurate lattices between group VIB TMDs and substrates are preferred, because of great challenges in theoretical simulations of coupled many-body systems. The recently explored 1H- VSe_2 is an ideal candidate for the purpose. As a family member of group VB TMDs, it shares a similar lattice constant with those of group VIB TMDs^{17,18}. Importantly, while it is paramagnetic in the bulk form, thin-film 1H- VSe_2 exhibits a ferromagnetic ground state, which remains stable above room temperature^{17,18}, rendering it a compelling platform for various high-temperature spintronic applications. For comparison, previous reported insulating magnetic substrates have a rather low Curie temperature, T_C . For example, the T_C 's of bulk EuO and EuS are 69K^{19,20} and 16.6 K²¹, while those of monolayer CrI_3 and $CrBr_3$ are around 45K²² and 34K²³, respectively. Further, the band edges of VSe_2 mainly contributed by V 3d orbitals are

close in energy to band edges of MSe_2 consisting of Mo/W d orbitals, suggesting the hopping and hybridization between these d orbitals with specific spin and thus the valley splitting could be tuned through external control knobs.

In this work, we present first-principles calculations on the magnetic proximity effect in MSe_2 ($M = Mo$ or W)/ VSe_2 heterostructures, demonstrating its manipulation by varying exchange interaction strength or strain. The energy alignment and hybridization between the valleys from MSe_2 and VSe_2 can be well tuned, leading to a large valley splitting of 29.1 meV in the topmost valence band of monolayer $MoSe_2$ and 55.8 meV in the second topmost valence band of monolayer WSe_2 , significantly larger than previous results. Moreover, a large valley splitting of 203 meV (202 meV) for the intralayer A (B) exciton in $MoSe_2$ and 156 meV for B exciton in WSe_2 is realized when the excitonic effect is taken into consideration.

Results And Discussions

Stacking registry and band alignment

The fully relaxed lattice constants for MSe_2 and VSe_2 are 3.32 Å and 3.33 Å, respectively, which indicates the lattice mismatch between these two monolayers is negligibly small. Thus, 1×1 primitive cells of monolayer MSe_2 and VSe_2 are stacked to form vdW MSe_2/VSe_2 heterostructures, with the in-plane lattice parameter fixed to 3.32 Å. Six high-symmetry stacking configurations are considered, which can be divided into two types, i.e., the R-type stacking with two layers sharing the same orientation and the H-type with two layers having opposite orientations, as shown in Fig. 1(a). To retain the C_3 rotational symmetry, the metal (M) site of MSe_2 layer can be vertically aligned with the V, Se, and hollow (h) sites of VSe_2 layer. The corresponding structures are named as $R(H)_V^M$, $R(H)_{Se}^M$, and $R(H)_h^M$, respectively. The equilibrium interlayer spacing d_0 's between two metal atoms in neighboring layers of the six stable stackings are listed in Supplementary Table 1. Clearly, the interlayer spacing d_0 's of R_V^M and H_h^M are larger than those of the other four stackings with slight difference. The characteristic features of R_V^M and H_h^M are one Se atom in MSe_2 is directly on top of another Se atom in the VSe_2 , resulting in the strong Coulomb repulsion between two layers.

Different stacking registries between the two constituents have important influences on the band offset in these heterostructures. Figure 1(b) shows the band alignments using PBE, HSE, GW@PBE and GW@HSE, which reveal strong dependence on the applied approximations. Specifically, both the $MoSe_2/VSe_2$ and WSe_2/VSe_2 show a type-III band alignment using the PBE method, even with the on-site Hubbard correction included for V d electrons. It is known that the alignment of valence band maximum (VBM) and conduction band minimum (CBM) with respect to the vacuum level are not accurate in the PBE level²⁴. More reasonable electronic structure can be achieved using hybrid functionals, in which a certain portion of the exact Hartree exchange is mixed with local or semilocal exchange²⁵. By varying the mixing coefficient α and range-separation Coulomb potential parameter μ , one can construct different HSE functionals incorporating different levels of exchange and correlation, denoted as HSE(α, μ). Hereafter, all HSE results are obtained using HSE ($\alpha = 0.1, \mu = 0.2 \text{ \AA}^{-1}$) unless noted otherwise. Under HSE level, both the $MoSe_2/VSe_2$ and

WSe₂/VSe₂ show a type-II band alignment. Further, many-body perturbation theory in GW approximation is a more practical routine to obtain band edges to compare with experimental data^{26–28}. To take into account the influences of exchange-correlation interaction on the electronic structure of magnetic VSe₂, two GW schemes, starting from either PBE or HSE functional results were chosen. The two GW schemes represent two different levels of exchange-correlation strength, which could be tuned by external fields, for example, strain^{29,30}. In particular, for MoSe₂/VSe₂, GW@PBE yields a type-I band alignment, whereas GW@HSE gives type-II band alignment, suggesting significant influences of exchange and correlation. These results indicate the positions of band edges from the two constituents of the heterostructures could feasibly be tuned, potentially leading to controllable hopping and hybridization strength.

Band structure and valley band splitting

The influences of interlayer orbital hybridization on the valley splitting is schematically presented in Fig. 2. With SOC, both the top valence band and bottom conduction band of MSe₂ split into two subbands, which are oppositely spin polarized but energetically degenerate at K and –K valleys, denoted by blue dashed lines in Fig. 2. The two valence and conduction bands for MSe₂ split by SOC are labeled as V1, V2 and C1, C2, while the nearest valence and conduction bands for VSe₂ are denoted as V1' and C1'. Assuming the ferromagnetic VSe₂ is spin-up polarized, there are two scenarios for orbital hybridization depending on the alignment between spin-polarized bands. When the V1 band of MSe₂ is closer to the V1' band of VSe₂, the effective interlayer hopping only happens between the MSe₂ V1 band and the VSe₂ V1' band at K, because of the requirement of spin conservation. The hybridization results in two mixed bands with orbital contributions from both MSe₂ and VSe₂, as depicted by solid lines in Fig. 2(a), leading to a considerable valley band splitting. Similarly, if the V2 band of MSe₂ matches well with V1' band of VSe₂, a significant *d-d* orbital hybridization appears between the MSe₂ V2 band and the VSe₂ V1' band only at –K, again resulting in notable valley splitting. Thus, the stacking-dependent interlayer coupling, the band alignment, and the spin conservation collaboratively determine the hybridization of electronic states, leading to varied valley splitting and rich excitonic structures.

Figures 3(a) and 3(b) show the calculated band structures for H_{Se}^M stacked MoSe₂/VSe₂ heterostructures using PBE and WSe₂/VSe₂ heterostructures under HSE level, respectively, while the results for the rest five stackings of MSe₂/VSe₂ are shown in the Supplementary Sec. II. Considering the band edges for MoSe₂ and WSe₂ at K and –K valleys are predominantly composed of transition metal d_{z^2} , d_{xy} and $d_{x^2-y^2}$ orbitals³¹, the weight decomposition of the contribution from these three orbitals is also provided in Figs. 3(a) and 3(b). It is clear that characteristic MSe₂ band edges are largely preserved in heterostructures. The calculated orbital projected band structures can also be used to estimate the band alignment between MSe₂ and VSe₂. For example, the metallic behavior obtained using PBE in Fig. 3(a) and Supplementary Figs. S2 and S3, suggests a type-III alignment, which is consistent with the previous band alignment calculations in Fig. 1(b).

Notably, in these heterostructures, different valleys are now imprinted by proximity exchange splittings. Focusing on the valence bands, the valley splitting energy is defined as the energy difference between the topmost valence bands (V1) or second topmost valence bands (V2) of MoSe₂ or WSe₂ at K and –K valleys,

that is, $\Delta E_{Vn} = E_K^{Vn} - E_{-K}^{Vn}$ with n equal to 1 or 2. The valley splitting values for six stable stackings are summarized in the Figs. 3(c) and 3(d), as well as the Supplementary Tables S2-S5. It can be found that the valley splitting in the heterostructures are strongly stacking dependent. Especially, the largest valley splitting under PBE approximation appears for the $V1$ band in H_{Se}^{Mo} stacked $MoSe_2/VSe_2$, reaching 29.1 meV, which is much larger than the reported values in WSe_2/CrI_3 and $MoSe_2/CrBr_3$ ^{6,7,15,16,32,33}. The large valley splitting is related to the strong valence bands hybridization between $MoSe_2$ $V1$ band and VSe_2 $V1'$ band at K point, which results in the significant contribution from Mo d orbitals to the original top valence band of VSe_2 as shown in Fig. 3(a). Such scenario corresponds to the scheme in Fig. 2(a). It can be further confirmed by the projected partial charge density distribution of the top two valence bands, which shows clear charge distribution over both $MoSe_2$ and VSe_2 layers (top panel of Supplementary Fig. S1). However, the hybridization is not allowed at $-K$ point, as a result of the opposite spin directions between VSe_2 $V1'$ and $MoSe_2$ $V1$ states at $-K$. For comparison, no hybridization emerges for H_{Se}^W stacked WSe_2/VSe_2 , due to the large energy mismatch in their valence band edges. In addition, H_h^M stacked $MoSe_2/VSe_2$ and WSe_2/VSe_2 show the smallest valley splitting. This is because they have the largest interlayer spacing, resulting in a weaker M-V proximity magnetic coupling. When the quasi-particle GW correction is taken into account, almost all the splitting values for both the valence and conduction bands become larger compared with PBE single-particle results (see Supplementary Tables S2 and S4).

Regarding to HSE results, similar enhancement is observed for most of the splitting values compared with PBE results [see Figs. 3(c) and 3(d)], except for H_{Se}^M stacked $MoSe_2/VSe_2$ owing to the vanished hybridization at K in HSE level (Supplementary Fig. S6). Furthermore, it is found that the valley splittings in WSe_2/VSe_2 are larger than those in $MoSe_2/VSe_2$. Such enhancement can be ascribed to the stronger hybridization between WSe_2 $V2$ band and VSe_2 $V1'$ band at $-K$ valley, where hole hopping from WSe_2 to VSe_2 is allowed for the aligned spin, as displayed in Fig. 3(b), which is in accordance with Fig. 2(b). In particular, ΔE_{V2} for H_{Se}^W stacked WSe_2/VSe_2 reaches 42.3 meV. Surprisingly, when GW approximation is applied on top of HSE, the splitting values does not increase overall (Supplementary Figs. S8 and S9). This may result from the combined effect of exchange interaction and the quasi-particle correction, which needs further exploration in the future.

Interlayer hybridization tuned by exchange interaction

As discussed above, the strongest splitting appears in H_{Se}^{Mo} stacked $MoSe_2/VSe_2$ within PBE method and H_{Se}^W stacked WSe_2/VSe_2 under HSE level ($\alpha = 0.1$, $\mu = 0.2 \text{ \AA}^{-1}$), with strong interlayer orbital hybridization. Such hybridization depends critically on the alignment of spin-polarized energy levels from two constituents of heterostructures, which are greatly influenced by exchange interaction. To unravel such effects, one can tune the hybridization strength adopting the hybrid functionals methods with varying parameters (α , μ), taking H_{Se}^M stacked heterostructures as examples in the following.

Figure 4 summarizes valley splitting values for H_{Se}^M at different α values. Considering the lowest-energy bright A exciton of WSe_2 ($MoSe_2$) originates from transition between $V1$ and $C2$ ($C1$) bands, the splittings for

WSe₂ C2 and MoSe₂ C1 are shown here. α coefficient dramatically changes the band alignment between the two layers (for more details, see Supplementary Figs. S10 and S11 as well as Tables S6 and S7). With increasing α , the CBMs at K and $-K$ move down, and become even lower in energy than original CBM at M when $\alpha = 0.15$, whereas the VBMs at K and $-K$ rise up, and become closer to VBM at Γ . The strongest hybridization emerges between MoSe₂ (WSe₂) V2 band and VSe₂ V1' band at $-K$ when α is around 0.06 (0.09). Meanwhile, the valley splittings of V2 band reach the maxima of 30.9 meV for MoSe₂ and of 55.8 meV for WSe₂, respectively. What's more, the strong hybridization can even give rise to the sign change of valley polarization, as shown in Fig. 4 for ΔE_{V2} , which leads to critical change in the transport and optical behaviors. Regarding μ parameter, the stronger the range-separated Coulomb potential (i.e., the smaller μ parameter) is, the larger the splitting is. Nevertheless, HSE calculations using different μ parameters give similar band structures (Supplementary Fig. S12), indicating that μ parameter does not affect much the interlayer hybridization.

The hybrid functionals involve a portion of exact exchange, and thus can also take the Hubbard U correction into account³⁴. To shed light on this point, the representative orbital projected band structures for MoSe₂/VSe₂ at varied U_{eff} values are plotted in Supplementary Fig. S13. For U_{eff} between 1.4 and 1.5 eV, valence bands show strong hybridization at $-K$ similar to the HSE cases with α around 0.06 (Supplementary Fig. S10). Because of its sensitivity to exchange and correlation effects, the actual ground-state band structures of the heterobilayers could depend on experimental conditions.

It should be pointed out that the tunability of the valley splitting through exchange interaction can be achieved experimentally. For example, one can feasibly apply an external pressure or in-plane strain onto the layered heterostructures to regulate the interlayer orbital hybridization. Applying strain/pressure can modify not only the interlayer distance or lattice constants but also the bandwidth, leading to the effective modulation of the electronic exchange and correlation interaction^{29,30,35,36}. To verify this, Supplementary Fig. S14 shows the band structures of heterostructures with a biaxial strain applied, which clearly display the change of band alignment and band hybridization.

Valley exciton splitting

The magnetic proximity effects in these heterostructures can be probed by their optical response, especially the valley intralayer exciton splitting of TMDs. In the absence of external magnetic field, the K and $-K$ valley excitons are degenerate in monolayer MSe₂, and the spectra (including peak shape and peak position) for left and right circularly polarized light show no difference. In the hybridized heterostructures, the effective hybridization at one valley renders the interband optical transition from either of the two hybridized valence bands to conduction band possible, as indicated by black and grey arrows in Fig. 2. While the transition at the other valley without hybridization is only allowed for bands contributed by one constitute layer.

Accordingly, strong splitting of the exciton states from K and $-K$ valleys emerges. The valley exciton splitting in TMDs is defined as the energy difference between low-energy bright A or B excitons from K and $-K$ valleys, i.e., $\Delta E^{A/B} = E_K^{A/B} - E_{-K}^{A/B}$. Figure 5 shows the optical absorbance of right and left circularly polarized light (σ_+ and σ_-) for the representative H_{Se}^M stacked heterostructures, while the rest are shown in Supplementary Figs. S15 and S16. The vertical solid blue and red lines denote the low-energy bright excitons

from K and $-K$ valleys, respectively. While the first two excitons are mainly contributed by VSe_2 monolayer, the four higher-energy excitons mostly originate from MSe_2 monolayers. Note that A and B exciton absorption peaks from MSe_2 monolayers already overlap with the continuum excitation of VSe_2 monolayer rather than well-separated ones. All heterostructures exhibit clear exciton valley splitting in MSe_2 monolayers except for the H_h^M stacked bilayers, which is consistent with its negligible electronic band valley splitting. The exciton valley splitting values are summarized in Supplementary Table S7.

It has been discussed in Sec. B that H_{Se}^M stacked $MoSe_2/VSe_2$ heterostructures shows a strong hybridization between topmost valence bands at K valley using PBE method, leading to a significant valley V1 band splitting. After taking into account the excitonic effects, it exhibits giant A exciton valley splitting reaching 203 meV, while B exciton shows slight splitting [see Fig. 5(a)]. In addition, the exciton splitting in VSe_2 monolayer is also enhanced by two fold³⁷. Under HSE ($\alpha = 0.06$, $\mu = 0.2 \text{ \AA}^{-1}$) approximation, a large B exciton splitting of 202 meV and a tiny A exciton splitting [Fig. 5(b)] appear, because of the effective hybridization between $MoSe_2$ V2 band and VSe_2 V1' band at $-K$. The hybridization pushes up the $MoSe_2$ V2 band, and at the same time moves down VSe_2 V1' band at $-K$, as depicted in Fig. 2(b). Accordingly, the $MoSe_2$ B exciton at $-K$ lies significantly below that at K valley, while the lowest-energy bright intralayer exciton in VSe_2 at $-K$ exceed the exciton at K in energy, leading to reversed exciton splitting in VSe_2 [compare Fig. 5(a) and Fig. 5(b)]. For H_{Se}^W stacked WSe_2/VSe_2 , A and B intralayer excitons in WSe_2 show almost comparable splitting [Fig. 5(c)] due to the absence of interlayer hybridization under PBE level. On the other hand, GW-BSE on top of HSE ($\alpha = 0.09$, $\mu = 0.2 \text{ \AA}^{-1}$), within which strong hybridization appears, gives rise to a large B exciton splitting of 156 meV similar to that of H_{Se}^M stacked $MoSe_2/VSe_2$.

To show the importance of the interlayer hybridization on excitonic transition, Supplementary Tables S8-S11 provide the decomposition of the exciton oscillator strength with respect to single particle transition for H_{Se}^M stacked heterobilayers. Under GW-BSE@PBE level, the lowest-energy bright exciton in $MoSe_2/VSe_2$ under σ -polarized light excitation denoted as $A_K^{VSe_2}$ exciton displays a considerable interlayer contribution from band V1 to C1', besides the main intralayer transition from band V1' to C1'. Meanwhile, for $A_K^{MoSe_2}$ exciton, the interlayer contribution from band V1' to C1 is comparable to the intralayer component from band V1 to C1 transition. Accordingly, $A_K^{VSe_2}$ and $A_K^{MoSe_2}$ excitons show hybridization between the corresponding intra- and interlayer exciton transitions because of the interlayer-hybridized hole. In contrast, $A_{-K}^{MoSe_2}$ exciton shows a negligible mixing with VSe_2 , due to the absence of effective band interlayer hybridization at $-K$. Eventually, there exists a large valley exciton splitting between $A_K^{MoSe_2}$ and $A_{-K}^{MoSe_2}$. Under HSE ($\alpha = 0.06$, $\mu = 0.2$) level, both $A_{-K}^{VSe_2}$ and $B_{-K}^{MoSe_2}$ exciton exhibits obvious mixed contributions from two monolayers, which significantly differs from $A_K^{VSe_2}$ and $B_K^{MoSe_2}$ excitons, leading to the significant B valley excitons splitting hitting 202 meV shown in Fig. 5(b). H_{Se}^W stacked WSe_2/VSe_2 shows the similar trend within GW-BSE@HSE.

These strongly hybridized intra- and interlayer excitons can emerge as new peaks below or above the A and B excitons in absorption and PL spectra, due to their strong oscillator strength inherited from the intralayer

exciton component³⁸. Meanwhile, because of their characteristic interlayer distribution, they could show a high tunability under external electric fields³⁹. Thus, the large exciton valley splitting can be observed in the MoSe₂ and WSe₂ monolayer via optical methods, which allows for the control and detection of magnetization using electrical or optical excitation.

Conclusions

In conclusion, using first principles methods we systematically investigated the valley splitting in MSe₂ on top of ferromagnetic monolayer VSe₂ to demonstrate a strong and tunable magnetic proximity effect. The magnitude of valley splitting relies on the strength of interlayer orbital hybridization and can be controlled feasibly by applying varied exchange and correlation interaction or in-plane strain. In principle, one can further tune the band offset by a vertical electric field to modulate the degree of hybridization⁴⁰. Remarkably, the control of interlayer exchange coupling could give rise to a strong intra- and interlayer exciton hybridization and sizable exciton valley splitting. Our study provides ideas for searching vdW heterostructures with giant valley splittings, and the proposed MSe₂/VSe₂ bilayers serve as excellent candidates for valleytronics research.

Methods

Our first principles calculations were carried out within the projector augmented wave method⁴¹ as implemented in VASP package⁴², with the generalized gradient approximation (GGA) functional of Perdew, Burke, and Ernzerhof^{43,44} adopted to describe the electron exchange and correlation effects. Electronic wave function was expanded on a plane-wave basis set with a kinetic energy cutoff of 400 eV. The convergence thresholds for electronic and ionic relaxations were chosen to be 1.0×10^{-7} eV and 0.001 eV/Å. The Brillouin zones for the heterostructures were sampled by 12×12×1 Γ -centered k-point meshes. The SOC effect was fully included in all our calculations and the van der Waals interaction was taken into account in the DFT-D3 scheme⁴⁵. The $3s^2 3p^6 4s^2 3d^8$ states of V, the $4s^2 4p^4$ of Se, the $5p^6 6s^2 5d^4$ of W and the $4s^2 4p^6 5s^1 4d^5$ of Mo were treated as valence states, respectively.

For hybrid functional calculations, the convergence thresholds for electronic minimizations were chosen to be 1.0×10^{-5} eV. The screened Coulomb potential by an inclusion of exact Hartree exchange could be simplified by using a mixing coefficient α and a range-separation Coulomb potential described by μ ⁴⁶. Dudarev et al.'s method⁴⁷ was also applied to treat localized V d electrons with the effective U parameter set as 1.13^{18,48}.

Single-shot GW (G_0W_0)²⁸ approach on top of both PBE (GW@PBE) and hybrid functional (GW@HSE) single-electron approximations were adopted for quasiparticle band structure calculations. For the monolayers and H_{Se}^M stackings, which are the main focus of our paper, more than 1000 bands were employed, while for the rest stackings a total number of empty bands more than twice the occupied bands were used. The optical properties were calculated by solving the Bethe-Salpeter Equation (BSE)^{49,50} based on GW correction. Fifteen

valence bands and fifteen conduction bands were included in the BSE optical transition calculations. The optical absorbance for circularly polarized light can be calculated from⁵¹

$$A(E) = \frac{Ed}{\hbar c} \text{Im}(\varepsilon_{xx} \pm i\varepsilon_{xy}), \quad (1)$$

where \hbar , c , E , d , ε_{xx} and ε_{xy} are the reduced Planck constant, the speed of light in vacuum, the energy of photon, the thickness of 2D heterostructures, the rescaled diagonal and nondiagonal terms of dielectric tensor for heterostructures, respectively. Im denotes the imaginary part of the dielectric tensor components. Considering the calculations for 2D heterostructures were performed under periodic boundary conditions with a sufficiently large interlayer distance $l = 30 \text{ \AA}$, the rescaled dielectric functions were obtained by eliminating the vacuum contribution through⁵²

$$\varepsilon_{xx} = 1 + \frac{l}{d} (\tilde{\varepsilon}_{xx} - 1), \quad (2)$$

$$\varepsilon_{xy} = \frac{l}{d} \tilde{\varepsilon}_{xy}, \quad (3)$$

where $\tilde{\varepsilon}_{xx}$ and $\tilde{\varepsilon}_{xy}$ are calculated dielectric functions of simulation cell with vacuum space.

Declarations

DATA AVAILABILITY

The datasets generated during and/or analyzed during the current study are available from the corresponding author on reasonable request.

ACKNOWLEDGMENTS

This work was supported by the National Natural Science Foundation of China (11974197 and 51920105002), Guangdong Innovative and Entrepreneurial Research Team Program (No. 2017ZT07C341), and the Bureau of Industry and Information Technology of Shenzhen for the 2017 Graphene Manufacturing Innovation Center Project (No. 201901171523).

AUTHOR CONTRIBUTIONS

D.W. were responsible for the calculations and data analyses. X.Z. and D.W. contributed to the discussion and the writing of the manuscript.

COMPETING INTERESTS

The authors declare no competing interests.

ADDITIONAL INFORMATION

Supplementary information The online version contains supplementary material available at https://doi.org/***.

Correspondence and requests for materials should be addressed to Xiaolong Zou.

References

1. Xiao, D., Liu, G. B., Feng, W., Xu, X. & Yao, W. Coupled spin and valley physics in monolayers of MoS₂ and other group-VI dichalcogenides. *Phys. Rev. Lett.* **108**, 196802 (2012).
2. Cao, T. *et al.* Valley-selective circular dichroism of monolayer molybdenum disulphide. *Nat. Commun.* **3**, 887 (2012).
3. Yu, H., Cui, X., Xu, X. & Yao, W. Valley excitons in two-dimensional semiconductors. *Nat. Sci. Rev.* **2**, 57–70 (2015).
4. Stier, A. V., McCreary, K. M., Jonker, B. T., Kono, J. & Crooker, S. A. Exciton diamagnetic shifts and valley Zeeman effects in monolayer WS₂ and MoS₂ to 65 Tesla. *Nat. Commun.* **7**, 10643 (2016).
5. Li, Y. *et al.* Valley splitting and polarization by the Zeeman effect in monolayer MoSe₂. *Phys. Rev. Lett.* **113**, 266804 (2014).
6. Hu, T. *et al.* Manipulation of valley pseudospin in WSe₂/CrI₃ heterostructures by the magnetic proximity effect. *Phys. Rev. B* **101**(2020).
7. Zollner, K., Faria, P. E. & Fabian, J. Proximity exchange effects in MoSe₂ and WSe₂ heterostructures with CrI₃: Twist angle, layer, and gate dependence. *Phys. Rev. B* **100**(2019).
8. Qi, J. S., Li, X., Niu, Q. & Feng, J. Giant and tunable valley degeneracy splitting in MoTe₂. *Phys. Rev. B* **92**(2015).
9. Li, Q. Z., Chen, K. Q. & Tang, L. M. Large Valley Splitting in van der Waals Heterostructures with Type-III Band Alignment. *Phys. Rev. Appl.* **13**(2020).
10. Scharf, B., Xu, G. F., Matos-Abiague, A. & Zutic, I. Magnetic Proximity Effects in Transition-Metal Dichalcogenides: Converting Excitons. *Phys. Rev. Lett.* **119**(2017).
11. Zhong, D. *et al.* Van der Waals engineering of ferromagnetic semiconductor heterostructures for spin and valleytronics. *Sci. Adv.* **3**, e1603113 (2017).
12. Zhang, S., Xu, R., Luo, N. & Zou, X. Two-dimensional magnetic materials: structures, properties and external controls. *Nanoscale* **13**, 1398–1424 (2021).
13. Norden, T. *et al.* Giant valley splitting in monolayer WS₂ by magnetic proximity effect. *Nature Communication* **10**, 4163 (2019).
14. Zhao, C. *et al.* Enhanced valley splitting in monolayer WSe₂ due to magnetic exchange field. *Nat. Nanotechnol.* **12**, 757–762 (2017).

15. Seyler, K. L. *et al.* Valley Manipulation by Optically Tuning the Magnetic Proximity Effect in $\text{WSe}_2/\text{CrI}_3$ Heterostructures. *Nano Lett.* **18**, 3823–3828 (2018).
16. Ciorciaro, L., Kroner, M., Watanabe, K., Taniguchi, T. & Imamoglu, A. Observation of Magnetic Proximity Effect Using Resonant Optical Spectroscopy of an Electrically Tunable $\text{MoSe}_2/\text{CrBr}_3$ Heterostructure. *Phys. Rev. Lett.* **124**(2020).
17. Bonilla, M. *et al.* Strong room-temperature ferromagnetism in VSe_2 monolayers on van der Waals substrates. *Nat. Nanotechnol.* **13**, 289–293 (2018).
18. Wang, X. *et al.* Ferromagnetism in 2D Vanadium Diselenide. *ACS Nano* **15**, 16236–16241 (2021).
19. Mauger, A. & Godart, C. The magnetic, optical, and transport-properties of representatives of a class of magnetic semiconductors: The europium chalcogenides. *Phys. Rep.-Rev. Sec. Phys. Lett.* **141**, 51–176 (1986).
20. Steeneken, P. G. *et al.* Exchange splitting and charge carrier spin polarization in EuO . *Phys. Rev. Lett.* **88**, 047201 (2002).
21. Zhao, F., Sun, H. L., Su, G. & Gao, S. Synthesis and size-dependent magnetic properties of monodisperse EuS nanocrystals. *Small* **2**, 244–248 (2006).
22. Huang, B. *et al.* Layer-dependent ferromagnetism in a van der Waals crystal down to the monolayer limit. *Nature* **546**, 270–273 (2017).
23. Zhang, Z. *et al.* Direct Photoluminescence Probing of Ferromagnetism in Monolayer Two-Dimensional CrBr_3 . *Nano Lett.* **19**, 3138–3142 (2019).
24. Jiang, H. & Shen, Y. C. Ionization potentials of semiconductors from first-principles. *J. Chem. Phys.* **139**, 164114 (2013).
25. Kummel, S. & Kronik, L. Orbital-dependent density functionals: Theory and applications. *Rev. Mod. Phys.* **80**, 3–60 (2008).
26. Shih, B.-C., Xue, Y., Zhang, P., Cohen, M. L. & Louie, S. G. Quasiparticle Band Gap of ZnO : High Accuracy from the Conventional $G(0)W(0)$ Approach. *Phys. Rev. Lett.* **105**(2010).
27. Aryasetiawan, F. & Gunnarsson, O. The GW method. *Rep. Prog. Phys.* **61**, 237–312 (1998).
28. Hybertsen, M. S. & Louie, S. G. Electron correlation in semiconductors and insulators: Band gaps and quasiparticle energies. *Phys. Rev. B* **34**, 5390–5413 (1986).
29. Li, S., Wang, Q., Zhang, C., Guo, P. & Yang, S. A. Correlation-driven topological and valley states in monolayer VSi_2P_4 . *Phys. Rev. B* **104**(2021).
30. Zhou, X. *et al.* Sign-reversible valley-dependent Berry phase effects in 2D valley-half-semiconductors. *Npj Comput. Mater.* **7**(2021).
31. Liu, G. B., Xiao, D., Yao, Y., Xu, X. & Yao, W. Electronic structures and theoretical modelling of two-dimensional group-VIB transition metal dichalcogenides. *Chem. Soc. Rev.* **44**, 2643–2663 (2015).
32. Zhong, D. *et al.* Layer-resolved magnetic proximity effect in van der Waals heterostructures. *Nat. Nanotechnol.* **15**, 187–191 (2020).
33. Zhang, Z., Ni, X., Huang, H., Hu, L. & Liu, F. Valley splitting in the van der Waals heterostructure $\text{WSe}_2/\text{CrI}_3$: The role of atom superposition. *Phys. Rev. B* **99**(2019).

34. Himmetoglu, B., Floris, A., de Gironcoli, S. & Cococcioni, M. Hubbard-Corrected DFT Energy Functionals: The LDA + U Description of Correlated Systems. *Int. J. Quantum Chem.* **114**, 14–49 (2014).
35. Gu, Y., Zhang, S. & Zou, X. Tunable magnetism in layered CoPS₃ by pressure and carrier doping. *Sci. China Mater.* **64**, 673–682 (2021).
36. Zhang, C. *et al.* Pressure-Enhanced Ferromagnetism in Layered CrSiTe₃ Flakes. *Nano Lett.* **21**, 7946–7952 (2021).
37. Tong, W. Y., Gong, S. J., Wan, X. & Duan, C. G. Concepts of ferrovalley material and anomalous valley Hall effect. *Nat. Commun.* **7**, 13612 (2016).
38. Alexeev, E. M. *et al.* Resonantly hybridized excitons in moire superlattices in van der Waals heterostructures. *Nature* **567**, 81–86 (2019).
39. Leisgang, N. *et al.* Giant Stark splitting of an exciton in bilayer MoS₂. *Nat. Nanotechnol.* **15**, 901–907 (2020).
40. Huang, D. & Kaxiras, E. Electric field tuning of band offsets in transition metal dichalcogenides. *Phys. Rev. B* **94** (2016).
41. Kresse, G. & Joubert, D. From ultrasoft pseudopotentials to the projector augmented-wave method. *Phys. Rev. B* **59**, 1758–1775 (1999).
42. Kresse, G. & Furthmüller, J. Efficiency of ab-initio total energy calculations for metals and semiconductors using a plane-wave basis set. *Comput. Mater. Sci.* **6**, 15–50 (1996).
43. Perdew, J. P., Burke, K. & Ernzerhof, M. Generalized gradient approximation made simple *Phys. Rev. Lett.* **78**, 1396–1396 (1997).
44. Zhang, Y. K. & Yang, W. T. Comment on "Generalized gradient approximation made simple". *Phys. Rev. Lett.* **80**, 890–890 (1998).
45. Grimme, S. Semiempirical GGA-type density functional constructed with a long-range dispersion correction. *J. Comput. Chem.* **27**, 1787–1799 (2006).
46. Heyd, J., Scuseria, G. E. & Ernzerhof, M. Hybrid functionals based on a screened Coulomb potential. *J. Chem. Phys.* **118**, 8207–8215 (2003).
47. Dudarev, S. L., Botton, G. A., Savrasov, S. Y., Humphreys, C. J. & Sutton, A. P. Electron-energy-loss spectra and the structural stability of nickel oxide: An LSDA + U study. *Phys. Rev. B* **57**, 1505–1509 (1998).
48. Fuh, H. R. *et al.* New type single-layer magnetic semiconductor in transition-metal dichalcogenides VX₂ (X = S, Se and Te). *Sci. Rep.* **6**, 32625 (2016).
49. Rohlfing, M. & Louie, S. G. Electron-hole excitations and optical spectra from first principles. *Phys. Rev. B* **62**, 4927–4944 (2000).
50. Rohlfing, M. & Louie, S. G. Electron-hole excitations in semiconductors and insulators. *Phys. Rev. Lett.* **81**, 2312–2315 (1998).
51. Molina-Sanchez, A., Catarina, G., Sangalli, D. & Fernandez-Rossier, J. Magneto-optical response of chromium trihalide monolayers: chemical trends. *J. Mater. Chem. C* **8**, 8856–8863 (2020).
52. Wu, M., Li, Z., Cao, T. & Louie, S. G. Physical origin of giant excitonic and magneto-optical responses in two-dimensional ferromagnetic insulators. *Nat. Commun.* **10**, 2371 (2019).

Figures

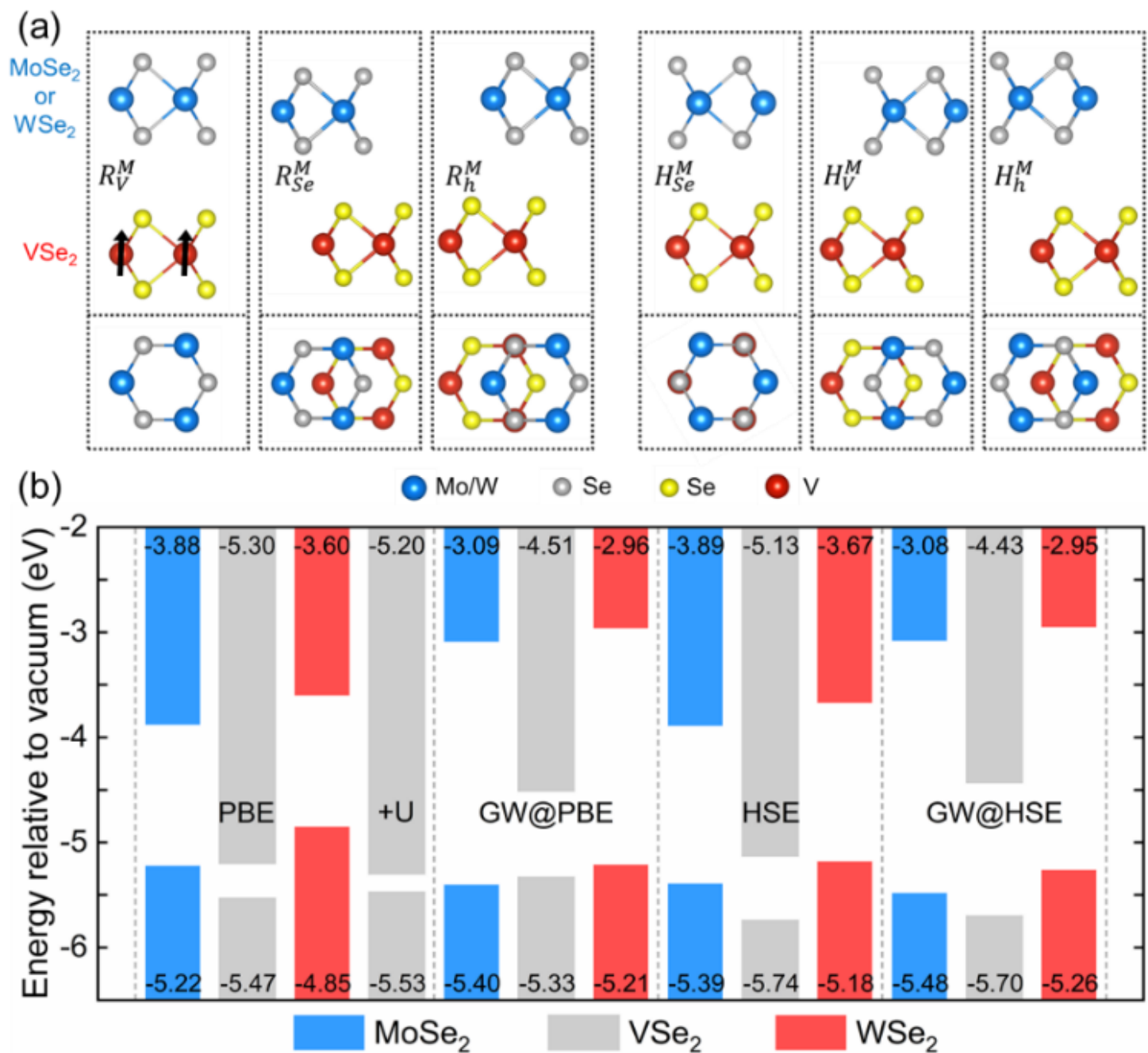


Figure 1

(a) Schematic top- and side-view of three R-type and three H-type heterobilayer registries. The Se atoms from MSe_2 and VSe_2 layers are shown in different colors. (b) Band edges relative to the vacuum energy level (set to zero) within different approximations for $MoSe_2$, WSe_2 and VSe_2 .

Figure 2

Schematic diagrams of two scenarios of interlayer hybridization. The energy levels for MSe_2 and VSe_2 before hybridization are shown by blue and red dashed lines, while hybridization between valence bands from MSe_2 and VSe_2 with aligned spin, lead to the hybridized bands indicated by solid colored lines. Two different scenarios are highlighted by the shadowed boxes. The corresponding band labels are shown to the right, with Vn/Cn (Vn'/Cn') denoting valence/conduction bands for MSe_2 (VSe_2). ΔE_{V1} and ΔE_{V2} are the valley bands splitting of the topmost valence band ($V1$) and second topmost valence band ($V2$) for MSe_2 . The short arrows alongside the bands represent spin direction. The resulting circularly polarized valley-split A and B excitonic transitions are also shown.

Figure 3

See image above for figure legend

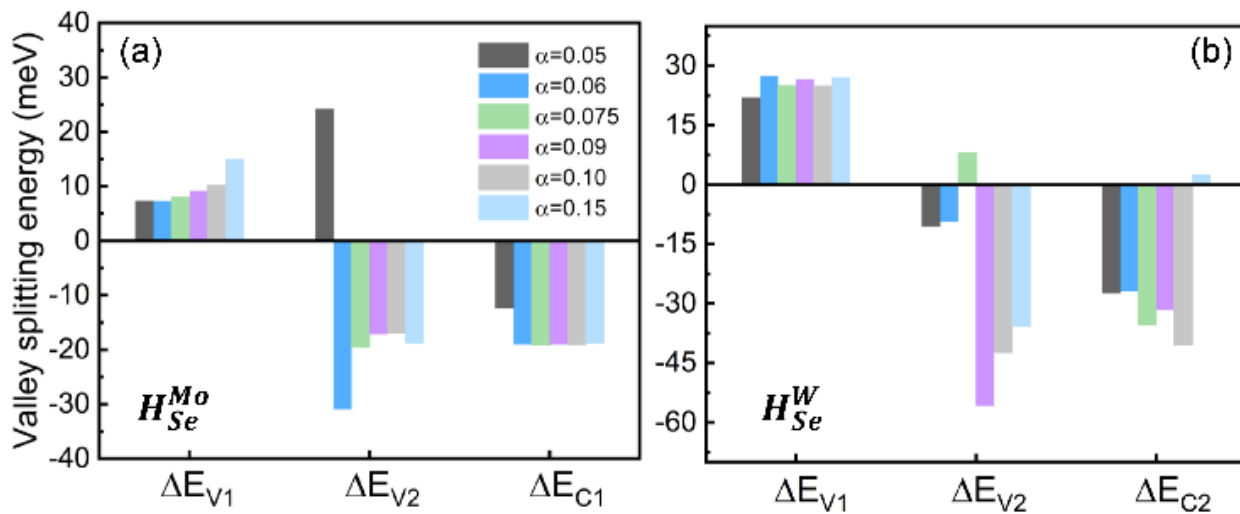


Fig. 4. The valley splittings ΔE_{V1} , ΔE_{V2} and $\Delta E_{C1(C2)}$ for the topmost valence band, the second topmost valence band and lowest conduction band (second lowest conduction band) of H_{Se}^M stacked $MoSe_2/VSe_2$ (a) and WSe_2/VSe_2 (b) using HSE with different α coefficients and fixed $\mu=0.2 \text{ \AA}^{-1}$.

Figure 4

See image above for figure legend

Figure 5

See image above for figure legend

Supplementary Files

This is a list of supplementary files associated with this preprint. Click to download.

- [SupplementaryinformationforTunablevalleybandandexcitonsplittingbyinterlayerorbitalhybridization.docx](#)